

One-Step Synthesis, Structure, and Band Gap Properties of SnO₂ Nanoparticles Made by a Low Temperature Nonaqueous Sol–Gel Technique

Mohamed Karmaoui,^{*,†,‡} Ana Belen Jorge,[§] Paul F. McMillan,^{||} Abil E. Aliev,^{||} Robert C. Pullar,[†] João António Labrincha,[†] and David Maria Tobaldi^{*,†}

[†]Department of Materials and Ceramic Engineering/CICECO—Aveiro Institute of Materials, University of Aveiro, Campus Universitário de Santiago, 3810-193 Aveiro, Portugal

[‡]Département de Génie Chimique, Faculté de Chimie, Université des Sciences et de la technologie Mohamed-Boudiaf El Mnaouer, BP 1505, Bir El Djir, 31000 Oran, Algeria

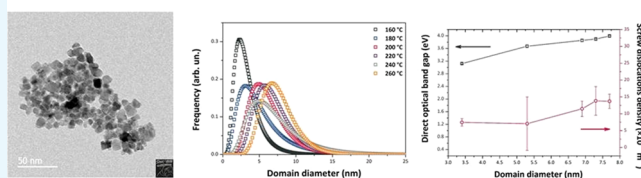
[§]Materials Research Institute, School of Engineering and Materials Science, Queen Mary University of London, Mile End Road, E1 4NS London, U.K.

^{||}University College London, Christopher Ingold Building, 20 Gordon Street, WC1H 0AJ London, U.K.

S Supporting Information

ABSTRACT: Because of its electrically conducting properties combined with excellent thermal stability and transparency throughout the visible spectrum, tin oxide (SnO₂) is extremely attractive as a transparent conducting material for applications in low-emission window coatings and solar cells, as well as in lithium-ion batteries and gas sensors. It is also an important catalyst and catalyst support for oxidation reactions. Here, we describe a novel nonaqueous sol–gel synthesis approach to produce tin oxide nanoparticles (NPs) with a low NP size dispersion. The success of this method lies in the nonhydrolytic pathway that involves the reaction between tin chloride and an oxygen donor, 1-hexanol, without the need for a surfactant or subsequent thermal treatment. This one-pot procedure is carried out at relatively low temperatures in the 160–260 °C range, compatible with coating processes on flexible plastic supports. The NP size distribution, shape, and dislocation density were studied by powder X-ray powder diffraction analyzed using the method of whole powder pattern modeling, as well as high-resolution transmission electron microscopy. The SnO₂ NPs were determined to have particle sizes between 3.4 and 7.7 nm. The reaction products were characterized using liquid-state ¹³C and ¹H nuclear magnetic resonance (NMR) that confirmed the formation of dihexyl ether and 1-chlorohexane. The NPs were studied by a combination of ¹³C, ¹H, and ¹¹⁹Sn solid-state NMR as well as Fourier transform infrared (FTIR) and Raman spectroscopy. The ¹³C SSNMR, FTIR, and Raman data showed the presence of organic species derived from the 1-hexanol reactant remaining within the samples. The optical absorption, studied using UV–visible spectroscopy, indicated that the band gap (E_g) shifted systematically to lower energy with decreasing NP sizes. This unusual result could be due to mechanical strains present within the smallest NPs perhaps associated with the organic ligands decorating the NP surface. As the size increased, we observed a correlation with an increased density of screw dislocations present within the NPs that could indicate relaxation of the stress. We suggest that this could provide a useful method for band gap control within SnO₂ NPs in the absence of chemical dopants.

Optical band gap (E_g) to lower energy with decreasing NP sizes



1. INTRODUCTION

As one of the most important members of the transparent conducting oxide (TCO) class of materials, the electronic and optical properties of pure and doped SnO₂ have been investigated extensively.^{1,2} Tin oxide (SnO₂) nanoparticles (NPs) are being developed for applications ranging from their incorporation as an opacifier in ceramic glazes to advanced technologies including gas sensors, lithium-ion batteries, low emission window coatings, touch screens, sensitized solar cells, field emission flat displays, and other optoelectronic devices.³ For each of these applications, it is important to have a simple,

low cost and scalable synthesis approach that will produce NPs within a narrow distribution of particle sizes.² Various synthesis strategies have been developed to produce SnO₂ NPs with different size ranges and distributions.^{4–11} These processes usually require use of high temperatures, high boiling point or mixed solvents, and expensive organic tin precursors that are often toxic and require a complicated synthesis procedure. The

Received: August 21, 2018

Accepted: October 1, 2018

55 experimental parameters required for such reactions run
 56 counter to the ability to produce highly crystalline nanosized
 57 structures with controllable properties. To avoid the problems
 58 associated with several of the proposed routes, synthetic routes
 59 that avoid the use of water and toxic solvents or surfactants
 60 and/or toxic solvents have been investigated.^{12,13} It is now
 61 important to develop one-pot synthesis methods that can
 62 produce crystalline SnO₂ NPs with tuneable particle sizes and
 63 band gap properties. Nonaqueous sol–gel processing is a
 64 flexible and powerful approach to obtain functionally active
 65 NPs.^{14–18} Here, we present a facile, one-pot, nonhydrolytic
 66 synthesis of SnO₂ NPs with controllable average size and with
 67 a narrow size distribution at low temperature.

68 Bulk crystalline SnO₂ with a tetragonal rutile structure
 69 (cassiterite phase) is an n-type direct gap semiconductor with
 70 the band gap (E_g) equal to 3.6 eV (344 nm). It provides an
 71 archetypal TCO, having up to 97% transparency across the
 72 visible spectrum.¹⁹ This large value is comparable with that
 73 required for complete transparency throughout the visible
 74 range (i.e., $E_g > 3.1$ eV). A large amount of research has been
 75 devoted to modifying the SnO₂ conduction band minimum
 76 and consequently modifying its optical absorption properties.
 77 These can be tuned by substituting elements such as such as F,
 78 Sb, or Pb on the anion or cation sites, by controlling NP size
 79 and morphology,^{1,2} or by causing internal strain within
 80 materials prepared as thin-film samples.²⁰ Nearly all of the
 81 studies to date have reported that E_g typically increases for
 82 smaller NP sizes.^{21–26}

83 The nonaqueous sol–gel process is based on the reaction
 84 between tin(IV) tetrachloride Sn(Cl)₄ and 1-hexanol, leading
 85 to the formation of SnO₂ NPs with a narrow dispersion and
 86 average sizes between 3.4 and 7.7 nm by varying the synthesis
 87 temperature between 160 and 260 °C. Both reagents are
 88 readily available, and the potentially scalable process yields NP
 89 materials that can be used without further processing.
 90 Unusually, we observed that E_g for our materials increased as
 91 the NPs became larger, with values determined to lie between
 92 2.22 (indirect) and 3.12 (direct) eV for 3.4 nm NP sizes, to
 93 3.53–3.99 eV for 7.7 nm particles. In order to investigate the
 94 origin of these unusual electronic structure changes, we carried
 95 out detailed structural and spectroscopic investigations of our
 96 SnO₂ NPs using a combination of X-ray powder diffraction
 97 (XRPD), high-resolution transmission electron microscopy
 98 (HRTEM), UV–visible, IR and Raman, and ¹¹⁹Sn, ¹³C, and ¹H
 99 nuclear magnetic resonance (NMR) spectroscopy techniques.
 100 Analysis of the XRPD data using the whole powder pattern
 101 modeling (WPPM) technique^{27–33} revealed the presence of
 102 axial strains and screw dislocations within the NPs. These
 103 strains are correlated with the presence of organic ligands
 104 detected by NMR, IR, and Raman spectroscopy and likely
 105 determine the unexpected band gap behavior, as well as
 106 providing possibilities for further modification and functional-
 107 ization of the NP surfaces.

2. RESULTS AND DISCUSSION

108 **2.1. X-ray Diffraction and HRTEM.** The SnO₂ NPs
 109 crystallized with the rutile structure (space group $P4_2/mnm$),
 110 with no additional impurity phases detected by X-ray
 111 examination (Figure 1). Initial examination of the XRPD
 112 patterns indicates that the peaks became sharper and better
 113 resolved with increasing NP size at higher synthesis temper-
 114 ature. We then applied WPPM analysis to the observed XRPD
 115 profiles.^{27,34} This approach provides information on the

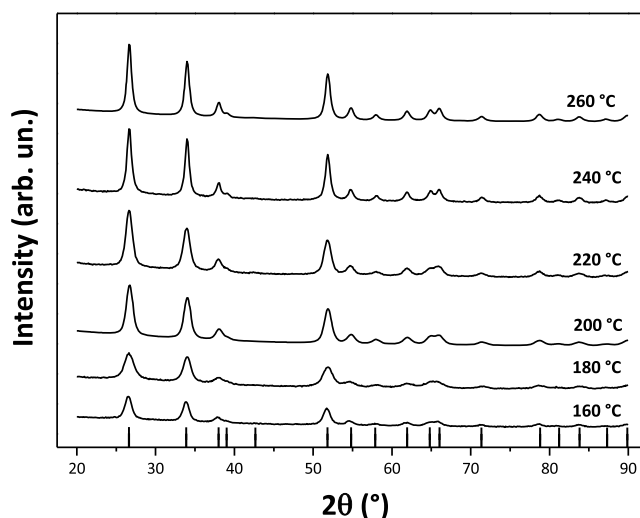


Figure 1. Powder X-ray diffraction patterns (Cu $K\alpha$ radiation) of the SnO₂ specimens prepared at different temperatures. The vertical lines below indicate the expected reflections for the rutile structured cassiterite phase.

average crystalline domain size of the SnO₂ NPs and edge
 and screw dislocation densities (Table 1 and Figure 2); it has
 also been applied recently to solve both size and defect
 concentration in the SnO₂ system.^{33,35,36} The almost flat
 nature of the residual line, displayed in Figure 2, indicates an
 excellent agreement between the experimental data and the
 model; this also suggests that the assumption of spherical
 shape for the investigated SnO₂ nanodomains is likely
 appropriate. The log-normal size distributions of the SnO₂
 NPs synthesized at different temperatures shown in Figure 3
 agree generally with the particle size distributions obtained
 from the HRTEM images described below. However, we note
 that the X-ray diffraction data and modeling provide more
 statistically representative sampling for the overall specimens
 than analysis of the TEM images. The unit cell volumes did
 not vary significantly as a function of synthesis temperature,
 but small changes in the tetragonal distortion of the SnO₂ unit
 cell were observed, primarily that the c/a ratio increased
 slightly with the increasing synthesis temperature (Table 1).
 The average crystalline domain diameter of SnO₂ at 160 °C
 found by WPPM analysis was 3.4 nm with a tail in the log-
 normal size distribution function extending to ~10 nm (Table
 1, Figure 3). Increasing the synthesis temperature led to a
 gradual increase in the average crystalline domain diameter—
 this became 6.9 nm at 220 °C and 7.7 nm by 260 °C. As
 shown in Table 1 and Figure 3, all the probability distributions
 have a positive skewness, with some dispersion around the tails
 to larger NP sizes. The number of screw dislocations “ ρ_e ” was
 determined to be greater than that of edge dislocations in all of
 the samples investigated (Table 1). The number of the edge
 dislocations did not change, whereas the density of screw
 dislocations “ ρ_s ” increased slightly as a function of the synthesis
 temperature.³³ The population of screw dislocations also
 exhibited a wider distribution about the mean for syntheses
 carried out at 180 °C (Figure 4).

The effects of synthesis temperature on the size,
 morphology, and development of defects within the SnO₂
 NPs were further investigated using HRTEM (Figure 5 and
 Table 2). All of the NPs exhibited a high degree of crystallinity,
 with lattice fringes matching the cell parameters of rutile-

Table 1. Results of WPPM Modeling and Refinement from the X-ray Powder Diffraction Data, Including Unit Cell Parameters, Tetragonality (c/a), Crystalline Domain Diameters (Average, Mode, and Skewness of the log-Normal Size Distribution), and Dislocation Densities (Edge and Screw, ρ_e and ρ_s , Respectively) of Synthesized SnO₂ NPs

synthesis temperature (°C)	agreement factors			unit cell parameters (nm)			c/a	crystalline domain diameter (nm)			dislocation density ($\times 10^{15} \text{ m}^{-2}$)	
	R_{wp} (%)	R_{exp} (%)	χ^2	$a = b$ (nm)	c (nm)	volume (nm ³)		average	mode	skewness	ρ_e	ρ_s
160	2.25	1.38	1.64	0.4751(1)	0.3185(1)	0.072(1)	0.6703	3.4(1)	2.3(1)	1.7(1)	1.0(7)	1.3(1)
180	1.85	1.34	1.38	0.4749(1)	0.3186(1)	0.072(1)	0.6709	5.3(2)	3.1(1)	2.2(1)	1.0(5)	1.2(8)
200	2.20	1.68	1.31	0.4750(1)	0.3189(1)	0.072(1)	0.6713	6.2(4)	4.9(3)	1.3(1)	1.0(7)	1.4(1)
220	1.94	1.33	1.46	0.4748(1)	0.3190(1)	0.072(1)	0.6719	6.9(2)	5.7(2)	1.1(1)	1.0(1)	1.7(2)
240	2.03	1.34	1.51	0.4748(1)	0.3188(1)	0.072(1)	0.6714	7.2(3)	5.0(2)	1.7(1)	1.0(3)	1.9(5)
260	2.04	1.31	1.56	0.4749(1)	0.3189(1)	0.072(2)	0.6714	7.7(1)	6.7(1)	0.9(1)	1.0(5)	1.9(2)

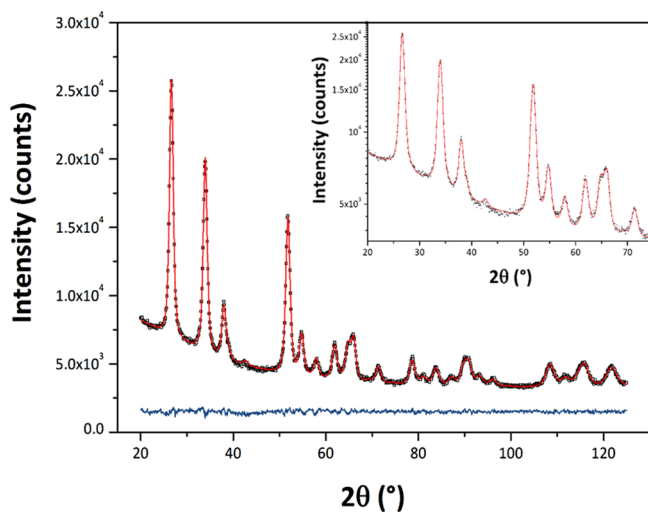


Figure 2. Typical output of the WPPM modeling protocol applied to the observed X-ray diffraction pattern of a specimen synthesized at 220 °C. The black open squares represent the observed data, and the red continuous line represents the refined fit. The blue continuous line below shows the difference between observed and calculated profile. The log-scale plot (up to 75° 2θ) shown in the inset highlights details in the peak tail and background region.

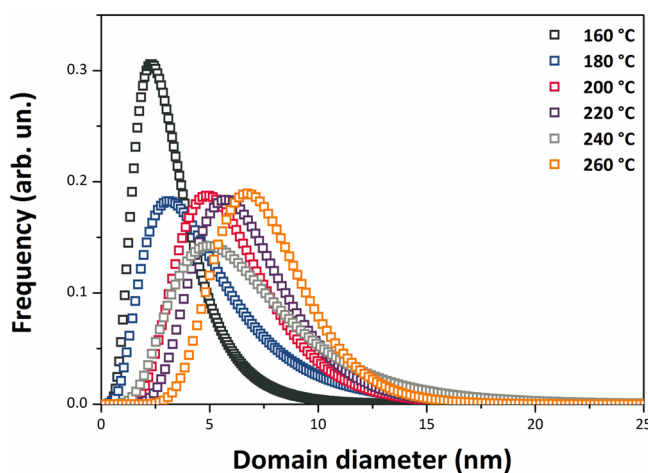


Figure 3. SnO₂ NP size distributions obtained from WPPM modeling.

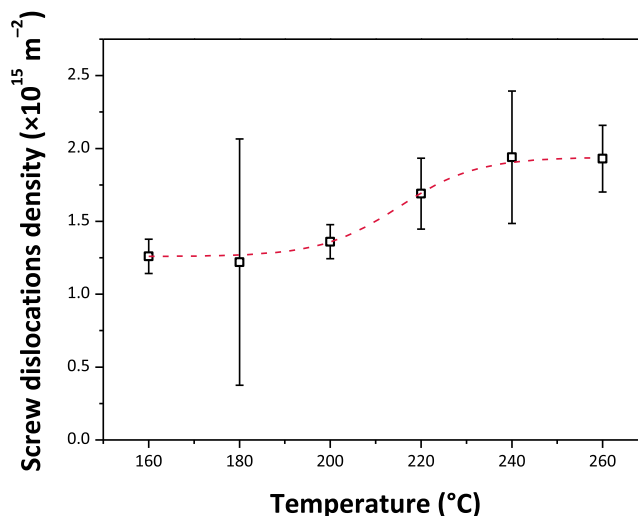


Figure 4. Evolution of screw dislocation densities with the synthesis temperature. The red dashed line represents a sigmoidal fit obtained using a sigmoidal Boltzmann function ($R^2 = 0.997$).

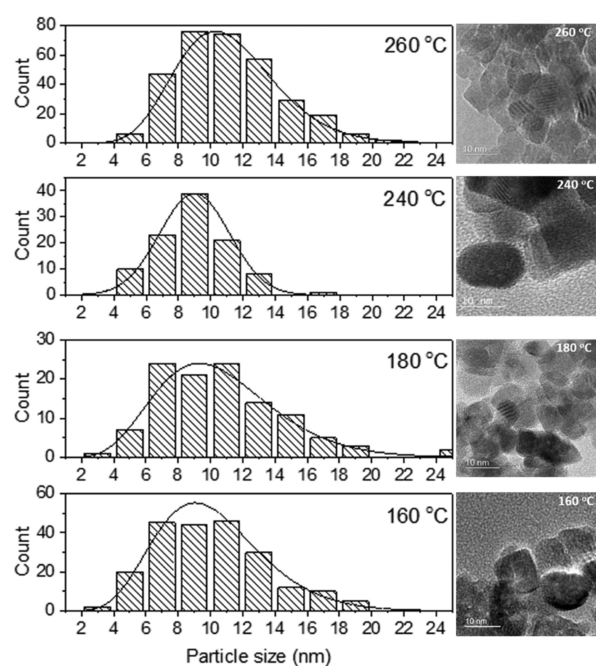


Figure 5. Particle size distribution (left) of SnO₂ NPs prepared at 160, 180, 240, and 260 °C from the analysis of HRTEM images (right).

156 structured SnO₂ (Figure 6). Our HRTEM images provided
 157 direct evidence for the existence of screw as well as edge
 158 dislocations within the SnO₂ NP samples deduced from the
 159 WPPM XRPD analysis (Figure 6). The SnO₂ crystallite sizes

Table 2. HRTEM Particle Size Distributions Obtained by Analysis of Images for Samples Prepared at 160, 180, 240, and 260 °C

temperature (°C)	average size (nm)	minimum size (nm)	maximum size (nm)	standard deviation
160	10.2	4.0	19.5	3.4
180	10.6	4.0	24.7	3.9
240	9.0	4.50	17.3	2.2
260	11.2	4.7	21.2	3.1

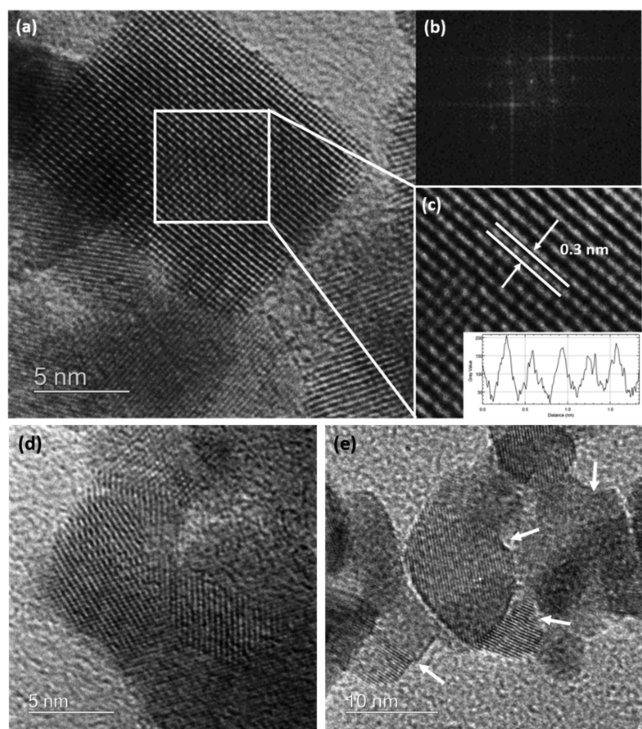


Figure 6. (a) HRTEM image of a SnO₂ sample prepared at 180 °C along with (b) its Fourier transform; (c) detail of the image showing lattice fringes with spacing ~0.3 nm corresponding to the *c* axis dimension of rutile structured SnO₂. Inset: Atomic density plot profile highlighting the spacing between lattice fringes; (d,e) HRTEM images showing the presence of screw and edge dislocations within NPs from this sample.

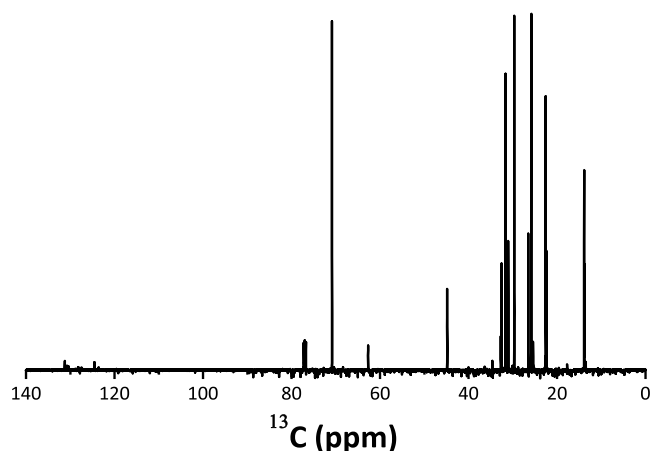


Figure 7. ¹³C NMR spectrum of the reaction solution after removal of the NPs.

solid-state ¹³C MAS NMR spectra, described in the following section.

2.3. Solid-State NMR of SnO₂ NPs. The ¹³C MAS NMR spectra of our samples are consistent with the production of 1-hexanol (C₆H₁₃OH), and also dihexyl ether (C₆H₁₃–O–C₆H₁₃) species during the SnO₂ NP synthesis reaction, that remain associated with the solid SnO₂ NP samples to the highest temperatures studied here. The spectrum of the sample prepared at 160 °C (Figure 8a) shows a broad signal at 64.9 ppm that can be assigned to the C1 atom of 1-hexanol. This is typically expected to occur at ~62 ppm, and the ~3 ppm increase in chemical shift can be attributed to strong H-bonding interactions with the SnO₂ NP surface. The 6 narrow signals observed at 72.5, 32.3, 30.1, 26.2, 23.1, and 13.3 ppm, 191

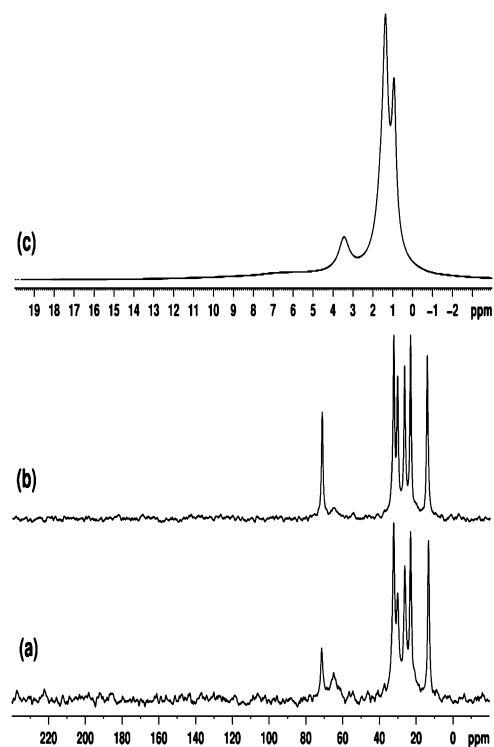


Figure 8. Proton-decoupled ¹³C MAS (8 kHz) SSNMR spectra of samples prepared at (a) 160 and (b) 200 °C; (c) ¹H MAS (12 kHz) NMR spectrum of the sample prepared at 200 °C.

160 estimated from the recorded images ranged between 2 and 11
161 nm, generally consistent with our WPPM analysis of the XRPD
162 data, although that analysis provides a more complete average
163 over the entire sample.

164 **2.2. Liquid Phase NMR Spectroscopy.** In order to study
165 the reaction of 1-hexanol with SnCl₄ during the synthesis, the
166 supernatant liquid was filtered to remove the SnO₂ solid
167 precipitate, and analyzed using liquid ¹H and ¹³C NMR
168 spectroscopy. The ¹³C NMR spectrum is shown in Figure 7
169 (the ¹H NMR spectrum is included in the Supporting
170 Information file, Figure S1). From the analysis of this
171 spectrum, the presence of 1-hexanol (with the C1 carbon at
172 62.8 ppm), dihexyl ether (with the C1 carbon at 71.1 ppm),
173 and 1-chlorohexane (with the C1 carbon at 45.1 ppm) was
174 determined (Table S1). All other peaks from these three
175 hydrocarbons corresponding to hexane carbons C2–C6 appear
176 in the same region at 14–33 ppm. The formation of the
177 dihexyl ether component was deduced from the analysis of the

192 along with analogous signals at 71.4, 32.5, 30.4, 26.6, 23.3, and
 193 14.3 ppm for the 200 °C sample, can be attributed to the 6
 194 inequivalent carbon environments (C1–C6) of the hexyl
 195 (C₆H₁₃–) fragments (Figure 8b). The observed shift at ~72
 196 ppm can suggest dihexyl ether formation due to the change
 197 from –CH₂–O–H to –CH₂–O–CH₂C₅H₁₁ environments.
 198 An additional β-effect of about +10 ppm of the CH₂C₅H₁₁
 199 substituent (by analogy with the β-effect of the methyl
 200 group)^{37–40} acting on the chemical shift of the C1 carbon
 201 would be consistent with this assignment. The reported ¹³C
 202 shifts for dihexyl ether in CDCl₃ solution at 71.05, 31.85,
 203 29.90, 26.01, 22.71, and 14.02 ppm^{37,38} agree with those
 204 observed here for samples prepared at 160 and 200 °C. Such
 205 high frequency shifts are well known from previous ¹³C NMR
 206 studies. The signals from C2–C6 atoms of dihexyl ether and 1-
 207 hexanol are expected to overlap.^{37–40} From Figure 8,
 208 increasing the synthesis temperature (*T*_{syn}) from 160 to 200
 209 °C leads to significant decrease of the signal intensity at ~65
 210 ppm, reflecting a decrease in the amount of adsorbed 1-
 211 hexanol at higher temperature. From the integral intensities of
 212 signals at 72 and 65 ppm, the mole-to-mole ratio of dihexyl
 213 ether to 1-hexanol changes from 0.6 at 160 °C to 2.7 at 200
 214 °C. Note that unlike the liquid-state ¹³C NMR spectrum
 215 (Figure 7), no signal was observed at ~45 ppm, indicating the
 216 absence of 1-chlorohexane in the ¹³C MAS SSNMR spectra of
 217 the SnO₂ NP samples analyzed (Figure 8).

218 The ¹H MAS spectrum of the sample prepared at 200 °C
 219 shows three well-resolved peaks at 3.4, 1.4, and 0.9 ppm
 220 (Figure 8c). The signals at 3.4 and 0.9 ppm are assigned to
 221 methylene and methyl protons of dihexyl ether. Signals from
 222 the remaining methylene protons of dihexyl ether (in positions
 223 2, 3, 4, and 5) overlap, giving rise to the signal with highest
 224 intensity at 1.4 ppm. A very broad peak at ~6 ppm can also be
 225 observed, that we assign to hydroxyl protons of water and 1-
 226 hexanol. The ¹H MAS spectrum of the sample prepared at 160
 227 °C was similar to that shown in Figure 8c, with slightly broader
 228 lines. The results definitely indicated the presence of dihexyl
 229 ether in the sample prepared at 260 °C. However, no 3.4 ppm
 230 signal was observed in the ¹H MAS spectrum of one sample
 231 prepared at 180 °C, that was subsequently annealed at 240 °C.

232 In order to gain insight into the structural differences
 233 between SnO₂ NPs synthesized at different temperatures, ¹¹⁹Sn
 234 SSNMR measurements were undertaken using 300 MHz
 235 (Figure 9) and 600 MHz NMR instruments. The half-height
 236 linewidths of the isotropic peaks in ¹¹⁹Sn MAS NMR spectra
 237 measured on a 600 MHz NMR instrument were as follows: 1.2
 238 ± 0.1 kHz (*T*_{syn} = 180 °C, annealed at 240 °C for 72 h) and 8
 239 ± 0.5 kHz (*T*_{syn} = 200 °C). Previously, Tunstall et al. measured
 240 ¹¹⁹Sn NMR parameters of a series of SnO₂ samples with
 241 powder sizes varying between 4 and 32 nm in comparison with
 242 data for standard bulk cassiterite SnO₂ powder (~10 μm)
 243 using a 500 MHz NMR spectrometer.⁴¹ In their case, the
 244 observed linewidths were between 0.6 and 1.7 kHz, which is
 245 significantly less than that measured in this work for our
 246 sample prepared at 200 °C.

247 We attribute such unusually large signal widths to the small
 248 average particle sizes achieved in our studies (<8 nm, where
 249 the sample properties are dominated by surface rather than
 250 bulk effects),⁴¹ combined with an increase in defect densities
 251 noted for the NPs from WPPM and HRTEM analysis. The
 252 linewidths of the isotropic peaks in ¹¹⁹Sn MAS NMR spectra
 253 measured on a 300 MHz NMR instrument were as follows: 3.5
 254 ± 0.2 kHz (*T*_{syn} = 160 °C), 0.68 ± 0.05 kHz (*T*_{syn} = 180 °C,

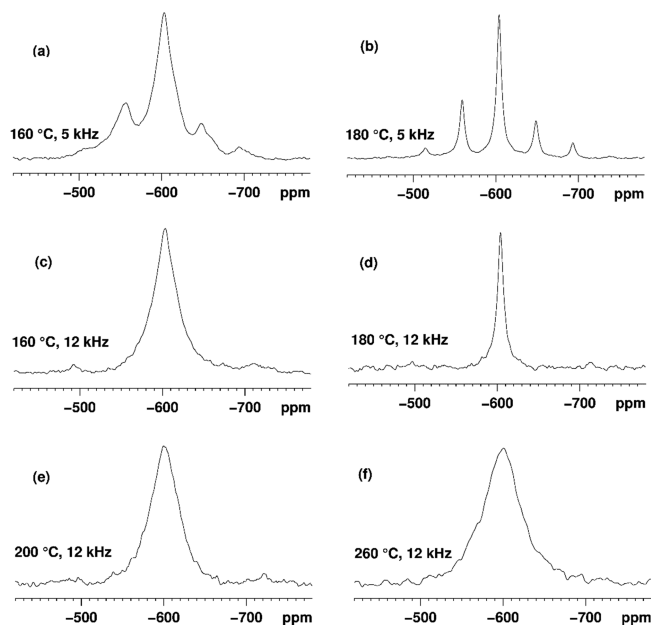


Figure 9. ¹¹⁹Sn MAS SSNMR spectra of SnO₂ samples prepared at (a) 160 °C (MAS 5 kHz); (b) 180 °C (MAS 5 kHz); (c) 160 °C (MAS 12 kHz); (d) 180 °C (MAS 12 kHz); (e) 200 °C (MAS 12 kHz); and (f) 260 °C (MAS 12 kHz). Unlike other samples, the sample prepared at 180 °C was subsequently annealed at 240 °C for 72 h.

then annealed at 240 °C for 72 h), 4.4 ± 0.2 kHz (*T*_{syn} = 200 °C), and 5.2 ± 0.5 kHz (*T*_{syn} = 260 °C). In previous work, the ¹¹⁹Sn NMR linewidths were found to increase with decreasing particle size. However, our results suggest the opposite behavior. This could be partly due to the increase in dislocation densities determined by WPPM analysis of our XRPD data. The observation of broad lines and their field dependence are also similar to those described by Alla and Lippmaa,⁴² which they attribute to the anisotropy of the magnetic susceptibility, Δχ_o. They showed that adamantane mixed at a 1:10 ratio with *p*-dibromobenzene shows severely broadened ¹³C lines due to the magnetic field produced by crystallites of *p*-dibromobenzene surrounding the adamantane particles. Similar arguments could apply in the case of SnO₂ NPs, where each ¹¹⁹Sn environment experiences the magnetic field produced by large numbers of smaller SnO₂ NPs, leading to broadened lines. Only the sample prepared at 180 °C and annealed at 240 °C shows narrow lines in the ¹¹⁹Sn NMR spectrum, and this is likely due to sintering of the NPs causing agglomeration into larger crystallites.⁴¹ There is a noticeable line narrowing on proton decoupling, giving rise to the following isotropic linewidths measured on a 300 MHz NMR instrument: 3.2 ± 0.2 kHz (160 °C), 0.67 ± 0.05 kHz (180 °C, annealed at 240 °C for 72 h), 4.1 ± 0.2 kHz (200 °C), and 4.9 ± 0.5 kHz (260 °C). This agrees with the ¹H and ¹³C NMR results that indicate that organic species and water are adsorbed on the surface of the SnO₂ NPs. The close proximity of protons to the tin atoms of SnO₂ leads to additional broadening due to ¹H–¹¹⁹Sn dipolar interactions in ¹¹⁹Sn MAS spectra without proton decoupling.

We estimated the ¹¹⁹Sn chemical shift anisotropy (CSA, Δδ) and the asymmetry parameter (η) for our samples.⁴³ As a reference, we used values for crystalline SnO₂, although we note that there is some disagreement in previously reported

¹¹⁹Sn CSA parameters for the cassiterite phase. Clayden et al.⁴⁴ reported $\Delta\delta/\eta$ values of -125 ppm/0, while Cossement et al.⁴³ found -125 ppm/0.27. From iterative Herzfeld–Berger analysis of the spinning sideband intensities using the HBA program^{43,44} in the ¹¹⁹Sn NMR spectrum recorded at a magic-angle spinning (MAS) frequency of 5 kHz at 7.05 T for the sample prepared at 180 °C, our best-fit $\Delta\delta/\eta$ values are -134 ppm/0.55, with $\delta_{11} = -535$ ppm, $\delta_{22} = -584$ ppm, $\delta_{33} = -693$ ppm, and $\delta_{\text{iso}} = -604$ ppm. These are in agreement with the best-fit $\Delta\delta/\eta$ values of -136 ppm/0.50 ($\delta_{11} = -536$ ppm, $\delta_{22} = -581$ ppm, $\delta_{33} = -695$ ppm, and $\delta_{\text{iso}} = -604$ ppm) determined from analysis of the ¹¹⁹Sn NMR spectrum recorded at a MAS frequency of 10 kHz at 14.1 T for the same sample. Our best-fit CSA parameters determined from the analysis of spinning sideband intensities at a MAS frequency of 5 kHz were $\Delta\delta = -131$ ppm and $\eta = 0.37$ ($\delta_{11} = -542$ ppm, $\delta_{22} = -575$ ppm, $\delta_{33} = -690$ ppm, and $\delta_{\text{iso}} = -603$ ppm) for the 160 °C sample and $\Delta\delta = -134$ ppm and $\eta = 0.50$ ($\delta_{11} = -535$ ppm, $\delta_{22} = -580$ ppm, $\delta_{33} = -691$ ppm, and $\delta_{\text{iso}} = -602$ ppm) for that prepared at 200 °C. Because of the very large linewidths, these can be only considered as approximate estimates, although they demonstrate an increase in values compared to those for bulk cassiterite^{43,44} with an average particle size ≈ 10 μm .⁴¹ Such changes in the ¹¹⁹Sn CSA parameters are commensurate with the increased number of Sn sites near the SnO₂ NP surface compared to bulk atoms in nanometer-sized NPs.

2.4. IR and Raman Spectroscopy. Fourier transform infrared (FTIR) spectra of the samples showed strong absorption occurring between 400 and 750 cm^{-1} with two main maxima observed near 650 and 545 cm^{-1} (Figure 10).

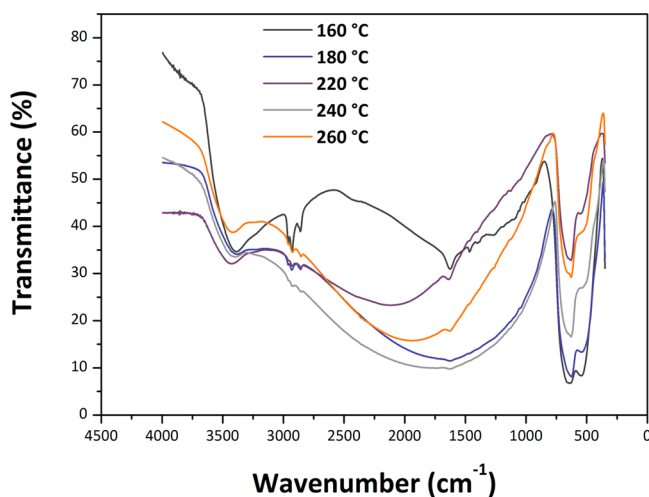


Figure 10. FTIR spectra of the samples containing SnO₂ NPs produced by the reaction between SnCl₄ and 1-hexanol at different temperatures.

These features are typical of SnO₂ NPs and are related to asymmetric and symmetric Sn–O stretching vibrations of the bulk phase.⁴⁵ The lower wavenumber component is slightly enhanced for samples prepared at lower temperature that have a smaller NP size, whereas an additional structure begins to be observed on the higher frequency band of the 260 °C sample, approaching the IR spectra of bulk SnO₂ powders.⁴⁶ The strong asymmetric band with its maximum near 3450 cm^{-1} indicates the presence of adsorbed molecular H₂O on the surface of the NP samples. This also gives rise to the feature

near 1630 cm^{-1} due to H–O–H bending. The SnO₂ NPs readily adsorb molecular H₂O from the atmosphere, as demonstrated by our thermogravimetric (TGA) analyses of samples that had been exposed to air (Figure S2).

The aliphatic C–H stretching peaks between 2850 and 2950 cm^{-1} confirm our NMR results that organic species derived from the 1-hexanol reactant remain present within the solid samples. These features are particularly strong for the sample synthesized at 160 °C, but they remain present to the highest synthesis temperatures studied here, suggesting that the organic species remain strongly bound to the external surfaces of the NPs. We do not yet have a good interpretation for the broad absorption feature observed between approximately 1000 and 3000 cm^{-1} , that has a maximum that moves to different wavelengths as a function of synthesis temperature, although it could be related to a light scattering effect associated with the dielectric SnO₂ NPs. Raman spectra were obtained for several series of SnO₂ NPs prepared in this study, using different instruments and excitation wavelengths. Representative data obtained with 514.5 nm laser excitation are shown in Figure 11. The spectra in the 400–700 cm^{-1} range are similar to observations by Diéguez et al.,⁴⁷ with broad bands dominated by surface rather than bulk modes (Figure 11b). Bulk crystalline SnO₂ with a tetragonal rutile structure (*P4₂/mnm* space group) exhibits four Raman active peaks due to zone center vibrations: A_{1g} (634 cm^{-1}), B_{2g} (773 cm^{-1}), E_g (473 cm^{-1}), and a low frequency (123 cm^{-1}) B_{1g} mode that is not reported in all studies. For highly crystalline materials including NPs with sizes above 75–100 nm, the spectra are dominated by the strong A_{1g} mode that becomes broadened and shift to a lower wavenumber as the particle size decreases.⁴⁸ The B_{2g} and E_g peaks become less visible, and broad features appear between 450–600 and 750–800 cm^{-1} , corresponding to vibrational excitations in the density of states function ($g(\omega)$) that become activated as the particle size is reduced. In addition, a weak peak due to a normally IR-active A_{2u} LO mode can be observed as a surface mode in larger NPs, while a further surface mode is reported to occur at 543 cm^{-1} .⁴⁸ As the NPs develop sizes below ~ 15 nm, a broad feature near 572 cm^{-1} begins to dominate the spectrum.^{47,49} This mode along with other weak features has also been associated with surface vibrations. Our spectra provide new information on features in the low wavenumber (200–400 cm^{-1}) region, which correspond roughly with the ($g(\omega)$) profile for the bulk crystalline phase.⁵⁰ Additional Raman features can also become activated because of the presence of defects, including screw dislocations, as shown by our X-ray WPPM analysis and HRTEM observations.⁵¹ Consistent with Diéguez et al.,⁴⁷ the A_{1g} mode broadens and shifts to a lower wavenumber as the NP size decreases, while the frequencies of B_{2g} and E_g modes approach that of the A_{1g} vibration. Our samples show broad bands in the 1350–1600 cm^{-1} range and near 3000 cm^{-1} because of the presence of 1-hexanol and dihexyl ether attached to the NP surface as detected by NMR spectroscopy.⁴⁷

2.5. UV–Visible Optical Spectroscopy and Band Gap Determination. UV–visible spectra were obtained for the SnO₂ NP samples using diffuse reflectance spectroscopy (DRS) (Figure 12). The UV–vis data were transformed into an absorbance scale by Kubelka–Munk analysis and optical E_g values determined using the Tauc method (Figure 13). The direct E_g for bulk SnO₂ occurs at 3.60 eV.^{51,52} For SnO₂ NPs, there is on-going discussion about the direct versus indirect

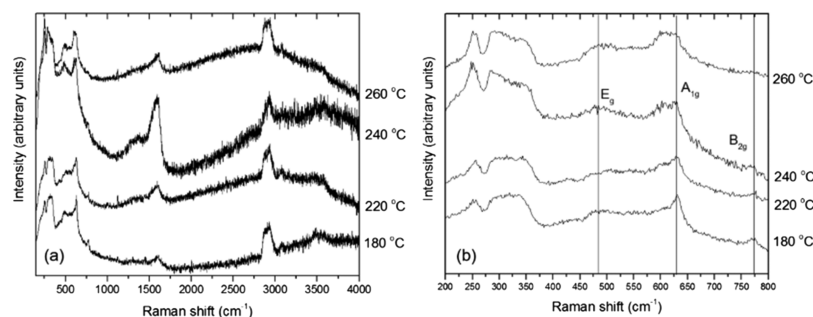


Figure 11. Raman spectra of SnO₂ samples prepared at 180, 220, 240, and 260 °C recorded using 514.5 nm excitation. (a) 200–4000 cm⁻¹ wavenumber range; (b) 200–800 cm⁻¹ wavenumber range.

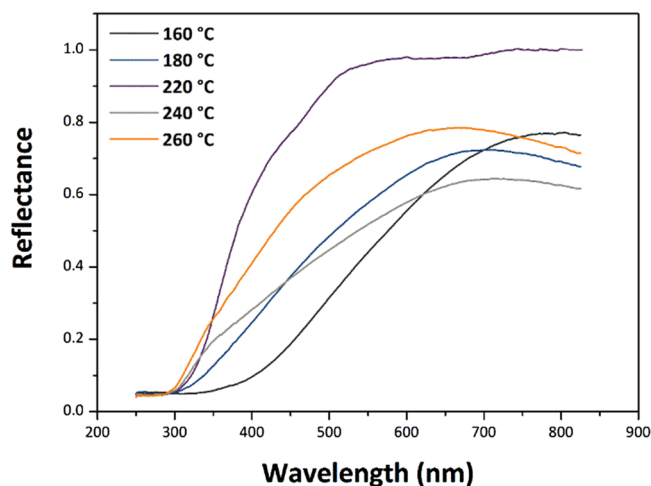


Figure 12. UV–vis diffuse reflectance spectra of SnO₂ NP specimens prepared at different temperatures.

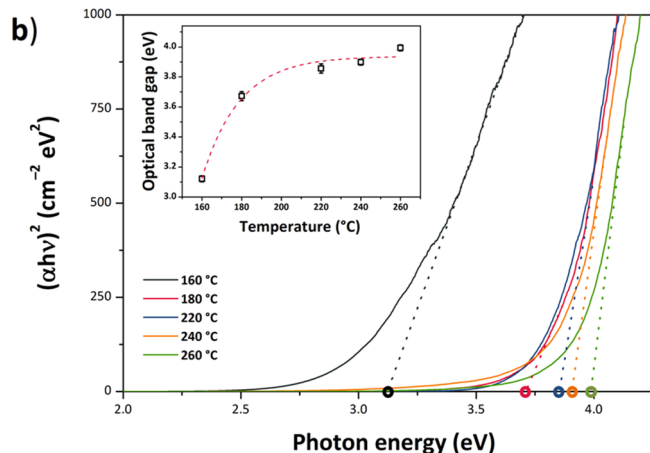
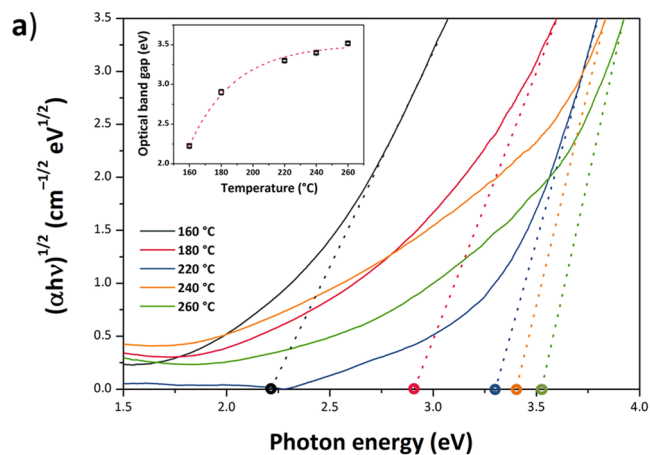


Figure 13. Plots of the Kubelka–Munk function vs photon energy of the specimens synthesized at different temperatures showing the optical E_g estimated using the Tauc procedure. The dashed lines represent the x -axis intercept of the line tangent to the inflection point for each dataset. (a) Indirect E_g model, $[F(R_\infty)h\nu]^{1/2}$, $\gamma = 2$. The insets show the systematic changes in E_g with increasing synthesis temperature and resulting NP size. (b) Directly allowed E_g model— $[F(R_\infty)h\nu]^2$, $\gamma = 1/2$; the red dashed lines are drawn as a guide for the eye, showing an approximately exponential trend for the evolution of the optical E_g with the increase in the synthesis temperature.

lattice strains could be linked to the presence of organic ligands derived from the synthesis procedure decorating the growing NP surfaces. The smallest NPs prepared at lowest temperature show the smallest axial strain values and both their direct and indirect E_g values are smaller than the bulk material. We can

393 nature of the interband transition.^{53–56} For this reason, we
 394 examined both $(\alpha h\nu)^2$ and $(\alpha h\nu)^{1/2}$ versus photon energy
 395 plots to determine E_g (Figure 13a,b). We note that the direct
 396 gap model yields E_g values that are systematically larger than
 397 with the indirect gap analysis, and it leads to values that exceed
 398 that of bulk SnO₂ for our NPs prepared at the highest
 399 temperatures. However, if the transition is indirect, it is found
 400 to approach the bulk value for the largest samples (Table 3). In
 401 both models, the E_g values increase with NP size and synthesis
 402 temperature. This observation contrasts with previous studies
 403 that have typically found an increase in the band gap of
 404 undoped SnO₂ NPs for smaller particle sizes.^{23,24,26,57} Here, we
 405 suggest an interpretation of our result based on the observed
 406 changes in structural parameters with NP size and preparation
 407 temperature, along with the presence of organic ligands derived
 408 from the synthesis decorating the NP surface.
 409 Our analyses of the XRPD data show that the NPs all have
 410 the same unit cell volume (0.072 nm³). This is approximately
 411 6–7% smaller than the bulk value (0.7687 nm³), indicating
 412 that our SnO₂ NPs are in a state of lattice compression
 413 compared with the bulk material. There is also a slight change
 414 in the a_0 and c_0 lattice parameters, with the smallest NPs
 415 prepared at lowest T_{syn} having the smallest c/a ratio (0.6703)
 416 rising to 0.6714 for the larger NPs (Table 1). Both values are
 417 larger than the value for bulk SnO₂ (0.6680), indicating a
 418 systematic increase in the degree of axial strain. Both tensile
 419 and compressive strains are known to modify E_g in SnO₂ and
 420 other semiconductors, as well as the direct versus indirect
 421 nature of the interband transition.^{20,58} We suggest that these

Table 3. Optical Band Gap (E_g) of the SnO₂ NP Specimens, as Calculated from the UV–Vis Data Using the Tauc Procedure

synthesis temperature (°C)	optical E_g (eV)	
	direct, $\gamma = 1/2$	indirect, $\gamma = 2$
160	3.12 ± 0.02	2.22 ± 0.02
180	3.67 ± 0.03	2.90 ± 0.03
220	3.86 ± 0.03	3.30 ± 0.02
240	3.90 ± 0.02	3.40 ± 0.02
260	3.99 ± 0.02	3.53 ± 0.02

relate this effect to the overall state of compression of the NPs, along with the c/a ratio that is 0.3% greater than the bulk material. As the NPs grow in size with higher synthesis temperature, we observe an increase in the c/a ratio along with an increased screw dislocation density (Figure 4, Table 1). The band gap shows a regular increase with the axial distortion, while the NPs remain in a similar compressed state, to either approach or exceed the bulk value depending on whether the transition is direct or indirect (Figure 14). The increased

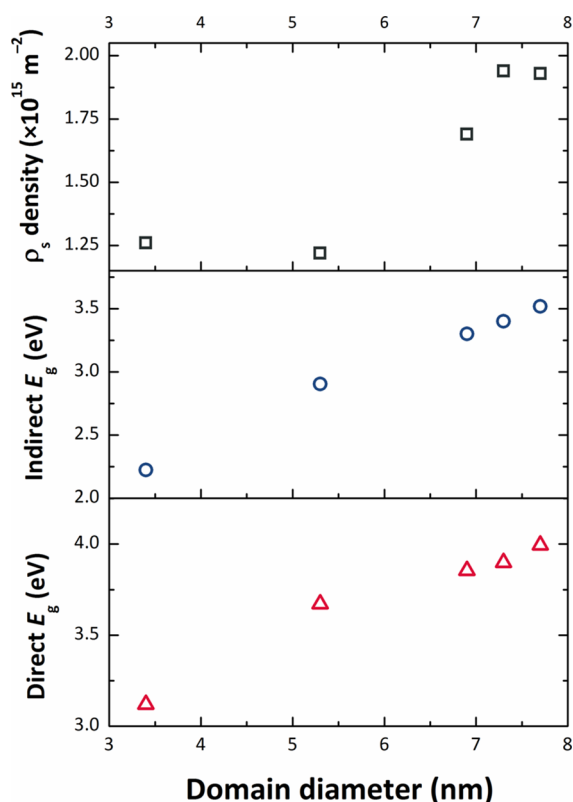


Figure 14. Evolution of the optical gap E_g (bottom panel: direct E_g vs domain diameter; middle panel: indirect E_g vs domain diameter) and the screw dislocation density with the average domain diameter (top panel).

concentration of screw dislocations determined by WPPM modeling of the XRPD data testifies to the presence of mechanical strains within the SnO₂ NPs synthesized by our low temperature nonaqueous sol–gel method (cf. Figure 14, top panel).

We also note that our UV–visible spectra show significant tailing effects at longer wavelengths, especially for the samples prepared at lowest T . This effect could be partly due to organic

ligands attached to the NP surface inducing ligand-to-metal charge transfer transitions⁵⁹ (Figure 12). Similar effects were noted by Wang et al. for carbon-coated SnO₂ NPs,⁶⁰ where the authors suggested that the outer carbonaceous layer could photosensitize SnO₂, extending the light absorption into the visible range. The absorption tails could also be associated with interband defect states associated with mechanical strains or O²⁻ vacancies within or at the surface of the NPs. We modeled the Urbach energies (E_u) associated with such possible defect states as ~ 278 meV.⁵¹

3. CONCLUSIONS

We have demonstrated a novel low-temperature (160–260 °C) solvothermal route to achieve crystalline SnO₂ NPs using a one-pot nonhydrolytic sol–gel synthesis method. The use of a readily available short chain alcohol (1-hexanol) as the reaction medium and as one of the reagents provides a potentially scalable process, leading to SnO₂ NPs with very small and controllable NP sizes within a narrow dispersion range. The reaction between SnCl₄ and 1-hexanol avoids the use of expensive and toxic precursors and thus offers an environmentally benign, inexpensive, and size-selected process for production of SnO₂ NPs with tunable optoelectronic properties. The nonaqueous sol–gel method, together with the WPPM analysis of XRPD data—combined with HRTEM imaging—allowed us to engineer functionally active NPs, determine the NP sizes, and identify screw dislocations present within the SnO₂ NPs in detail. This was further confirmed by HRTEM imaging.

We studied changes in the optical band gap E_g by analysis of UV–visible spectroscopic data. Our results indicated that E_g was smaller than that for bulk SnO₂ for the smallest particles but increased with NP size, contrary to previous findings. If we assumed a direct gap model for interband transitions, our value estimated for >3.5 nm particles exceeded that of the bulk solid, whereas indirect gap analysis showed values approaching the bulk for larger NPs prepared at higher temperature. We suggest that the unexpected variation in E_g with a NP size is due to internal strain parameters developed within the NPs that also lead to an increase in screw dislocation densities observed at higher temperatures, as the particles become larger. The internal strains may be associated with the presence of organic ligands attached to the growing NP surfaces derived from the synthesis reaction. Our simple, low-cost synthetic method leads to new possibilities for tailoring the E_g of SnO₂ nanomaterials as a function of NP size, surface decoration, and the presence or relaxation of internal mechanical strains. Such an approach can allow further tuning of the electronic properties and visible light transparency of SnO₂ NPs for optoelectronic devices.

4. EXPERIMENTAL SECTION

4.1. Synthesis of SnO₂ NPs. Tin(IV) chloride (99.995%) and anhydrous 1-hexanol (99%) were used as obtained from Aldrich. The syntheses were carried out in a glovebox under controlled environmental conditions (O₂ and H₂O < 1 ppm). In a typical procedure, 1 mmol (0.2603 g) of tin(IV) chloride was added to 20 mL of 1-hexanol, and the mixture was transferred into a stainless-steel autoclave and sealed. The autoclave was taken out of the glovebox and heated in a furnace at between 160 and 260 °C for 3 days. The resulting milky suspensions were centrifuged, and the precipitates were

502 washed with ethanol and dichloromethane and dried in air at
503 60 °C.

504 **4.2. Sample Characterization.** The SnO₂ NPs were
505 studied by XRPD using a θ/θ diffractometer (PANanalytical
506 X'Pert Pro, NL) equipped with a fast RTMS detector, using
507 Cu $K\alpha$ radiation (45 kV, 40 mA), in the 20–125° 2θ range,
508 with a virtual step scan of 0.1° 2θ , and a virtual time per step of
509 500 s. The diffraction profiles were analyzed via the WPPM
510 approach,^{27–33} using the PM2K software suite.³⁴ This powerful
511 new technique allows extraction of microstructural information
512 from a powder diffraction pattern, by refining model
513 parameters via a nonlinear least squares fitting routine, fit to
514 the experimental data profile. Within the WPPM method, there
515 is no need for modeling the data using arbitrary peak shape
516 functions (e.g., Gaussian, Lorentzian, and Voigt), as the
517 experimental scattering profile is fit as a convolution of
518 instrumental and sample-related physical effects. In this way,
519 the structural analysis is developed by taking into account
520 physical models of not only the lattice parameters but details of
521 the microstructure and lattice defects including planar and
522 screw dislocations.^{27–34} The WPPM method provides an
523 assessment of all aspects of the microstructure including the
524 crystallite domain shape, size, and distribution, with effects due
525 to dislocations modeled through the description of a
526 dislocation contrast factor in terms of a crystallographic
527 invariant.^{29,32} It provides considerably more detailed informa-
528 tion compared with other integral methods for line profile
529 analysis of XRPD data, such as the routinely used Scherrer
530 formula,⁶¹ or the Williamson–Hall approach.⁶² In these
531 methods, instrumental profile components, background and
532 peak profile overlap can play an unwanted role in correctly
533 extracting integral breadths.^{61,62} Furthermore, additional
534 sources of line broadening and peak asymmetry, including
535 domain size, lattice strain, and the presence of lattice defects,
536 cannot be investigated in detail.⁶³ Here, the instrumental
537 contribution to the XRPD profile was calibrated by modeling
538 14 hkl reflections from the NIST SRM 660b standard (LaB₆),
539 according to the Caglioti et al. relationship.⁶⁴ Then, SnO₂
540 described within space group $P4_2/mnm$ for the tetragonal rutile
541 structure was introduced in the WPPM modeling of the data,
542 and the following parameters were refined: background
543 (modeled using a 4th-order shifted Chebyshev polynomial
544 function), peak intensities, specimen displacement, mean and
545 variance of the NP size distributions, and lattice parameters.
546 For simplicity, the crystalline diffracting domains were
547 assumed to be spherical and that their diameter was distributed
548 according to a log-normal size distribution. Both edge and
549 screw dislocations having densities of ρ_e and ρ_s , respectively,
550 were initially assumed to be present in the $10\bar{1}\{101\}$ slip
551 system, as was shown by Koffyberg [Burgers vector equal to
552 $(a_0^2 + c_0^2)^{1/2}$, with a_0 and c_0 being the lattice parameters],⁶⁵
553 and validated recently by Scardi's group by means of the
554 WPPM method.^{33,35} Our HRTEM images (see below) showed
555 that screw dislocations constituted the main defect observed in
556 the NPs, and hence, these were considered to be the only
557 source of anisotropy in the XRPD line profile broadening.

558 Transmission electron microscopy (TEM) was performed
559 using a Jeol-2000 FXII microscope, with point-to-point and
560 line-to-line resolutions of 0.28 and 0.14 nm, respectively.
561 Additional high-resolution TEM (HRTEM) images were
562 obtained using a JEOL 2200FS microscope with a field-
563 emission gun, operated at 200 kV. Samples for TEM/HRTEM
564 observations were prepared by dispersing the NPs in ethanol

and methanol, respectively, and evaporating the suspension
565 drops on carbon-coated Cu grids. 566

FTIR spectra were obtained using a Bruker Tensor 27
567 spectrometer. The IR measurements were carried out over the
568 wavenumber range 4000–350 cm⁻¹. Sample powders (2 mg)
569 were mixed with KBr (200 mg, to give ~1 wt % of powder in
570 the KBr disks) and pressed into thin pellets. Raman spectra
571 were measured using a Renishaw micro-Raman instrument
572 with excitation wavelengths of 325 and 514.5 nm. DRS was
573 used to evaluate the optical properties of SnO₂ in the UV–
574 visible range. Spectra were acquired using a Shimadzu UV
575 3100 (JP) spectrometer equipped with a BaSO₄ integrating
576 sphere in the 825–250 nm range, with 0.2 nm in step size, and
577 using BaSO₄ as white reference material. The diffuse
578 reflectance data (R_∞) were converted into an absorption
579 coefficient α using the Kubelka–Munk transformation⁶⁶ 580

$$\alpha \approx \frac{k}{S} = \frac{(1 - R_\infty)^2}{2R_\infty} \equiv F(R_\infty)$$

Here, k is the wavelength-dependent absorption coefficient (k
581 = $4\pi\kappa/\lambda$) and S is a scattering coefficient, assumed to be
582 constant over the wavelength range. The optical band gap E_g
583 of the SnO₂ NPs was assessed by the Tauc procedure that
584 assumes the absorption coefficient α of a semiconductor can be
585 expressed as 586

$$(\alpha h\nu) = A(h\nu - E_g)^\gamma$$

where A is a material-dependent constant, h is Planck's
587 constant, and ν is the light frequency. The power coefficient γ
588 is characteristic of the type of transition considered, with a
589 value of 1/2 or 2 depending on whether the transition is
590 directly or indirectly allowed.⁶⁷ There is still not agreement on
591 whether the band-to-band transition in SnO₂ NPs is direct or
592 indirect.^{7,53,54} We tested both solutions to estimate E_g values in
593 our study. We fitted the plots given by the transformed
594 Kubelka–Munk equation $[F(R_\infty)h\nu]^\gamma$ versus $h\nu$ using a
595 sigmoidal Boltzmann function (Origin ProLab, version
596 8.5.0). The x -axis intercept of the line tangent to the inflection
597 point of the appropriate curve provided direct versus indirect
598 gap model estimates for each of our SnO₂ NP samples. 599

Liquid-state ¹H and ¹³C NMR spectroscopies were used to
600 investigate the organic species formed during the reaction and
601 remaining in the supernatant liquid after centrifugation. 602
603 Spectra were measured in CDCl₃ solutions using a 300 MHz
604 Bruker AVANCE NMR spectrometer. Solid-state NMR
605 experiments to study the SnO₂ NPs were carried out at
606 ambient probe temperature on a Bruker AVANCE 300
607 spectrometer with a 7.05 T wide-bore magnet. High-resolution
608 solid-state ¹H, ¹³C, and ¹¹⁹Sn NMR spectra were recorded at
609 300.1, 75.5, and 111.9 MHz, respectively, using a standard
610 Bruker 4 mm double-resonance MAS probe. Powdered solid
611 materials were packed into zirconia rotors of 4 mm external
612 diameter and spun at MAS frequencies of 3–12 kHz with
613 stability better than ± 3 Hz. High-resolution solid-state ¹³C
614 NMR spectra were recorded using MAS, with high-power
615 proton decoupling and the pulse sequence of Cory and
616 Ritchey⁶⁸ with the suppression of extraneous signals
617 originating from materials outside the NMR coil. Typical
618 acquisition conditions for ¹³C NMR experiments were as
619 follows: ¹³C 90° pulse duration = 3.0 μ s; recycle delay = 10 s;
620 number of transients 6000–17 200. Solid-state ¹³C MAS
621 spectra with high-power proton decoupling and cross-polar-

ization (CP) from protons were also acquired for the sample prepared at 200 °C, with the following acquisition conditions: ^1H 90° pulse duration = 4.0 μs ; recycle delay = 5 s; and number of transients 3400. However, the ^{13}C CPMAS spectrum showed a poorer signal-to-noise ratio compared to that acquired using the sequence of Cory and Ritchey⁶⁹ with the direct detection of ^{13}C nuclei. Solid-state ^{119}Sn MAS spectra at 111.9 MHz with and without high-power proton decoupling were recorded using the following acquisition conditions: ^{119}Sn 60° pulse duration = 1.5 μs ; recycle delay = 10–30 s; number of transients 2000–30 000, and MAS frequency = 3–12 kHz. Additionally, ^{119}Sn SSNMR spectra were recorded on a Bruker AVANCE 600 MHz spectrometer at the resonance frequency of 223.8 MHz using the following acquisition conditions: ^{119}Sn 45° pulse duration = 2.0 μs ; recycle delay = 5 s; number of transients 1500–12 300, and MAS frequency = 10–12 kHz. The sequence used to collect ^1H MAS NMR spectra at 300.1 MHz comprised a single-pulse excitation with a 2.4 μs long pulse (recycle delay = 5 s; number of transients 8–32, and MAS frequency = 8–12 kHz). The ^{13}C and ^1H chemical shifts are given relative to tetramethylsilane (TMS), which were calibrated using glycine (176.46 ppm) and tetrakis(trimethylstannyl)methane doped with TMS (0 ppm), respectively. The ^{119}Sn chemical shifts are given relative to tetramethyltin SnMe_4 , calibrated using tetrakis(trimethylstannyl)methane $\text{C}(\text{SnMe}_3)_4$ (48.2 ppm).⁶⁹ In the case of the ^{119}Sn CSA ($\Delta\delta$) for SnO_2 with $\delta < 0$, parameters are defined as follows

$$\text{Principal CSA components } \delta_{11} \geq \delta_{22} \geq \delta_{33}$$

$$\text{Isotropic value } \delta_{\text{iso}} = (\delta_{11} + \delta_{22} + \delta_{33})/3$$

$$\text{Chemical shift anisotropy } \Delta\delta = \delta_{33} - (\delta_{11} + \delta_{22})/2$$

$$\text{Asymmetry parameter } \eta = (\delta_{22} - \delta_{11})/(\delta_{33} - \delta_{\text{iso}}) \text{ with } 0 \leq \eta \leq 1$$

Here, the principal components of the chemical shift tensor, δ_{11} , δ_{22} , and δ_{33} , are defined such that the highest frequency (the least shielded) component is labeled as δ_{11} , while δ_{33} corresponds to the lowest frequency (the most shielded) component.

ASSOCIATED CONTENT

Supporting Information

The Supporting Information is available free of charge on the ACS Publications website at DOI: 10.1021/acsomega.8b02122.

^1H NMR spectrum of the filtered reaction solution measured in CDCl_3 of the SnO_2 NPs; TGA of the SnO_2 NP samples synthesized at different temperatures; and ^{13}C NMR chemical shift values for key organic species discussed in the text (PDF)

AUTHOR INFORMATION

Corresponding Authors

*E-mail: karmaoui@ua.pt, karmaoui.mohamed@univ-usto.dz, m.karmaoui@surrey.ac.uk (M.K.).

*E-mail: david.tobaldi@ua.pt, david@davidtobaldi.org (D.M.T.).

ORCID

Mohamed Karmaoui: 0000-0002-2288-6290

Paul F. McMillan: 0000-0002-5298-780X

Robert C. Pullar: 0000-0001-6844-4482

David Maria Tobaldi: 0000-0002-0112-8570

Notes

The authors declare no competing financial interest.

ACKNOWLEDGMENTS

M.K. thanks Fundação para a Ciência e a Tecnologia (FCT) for grant no. SFRH/BPD/74477/2010. This work was developed within the scope of the project CICECO–Aveiro Institute of Materials, POCI-01-0145-FEDER-007679 (FCT Ref. UID/CTM/50011/2013), financed by national funds through the FCT/MEC and when appropriate co-financed by FEDER under the PT2020 Partnership Agreement. R.C.P. thanks FCT grant IF/00681/2015 for supporting this work. Dr Harold Toms is thanked for assistance performing SSNMR measurements.

DEDICATION

We dedicate this work to the memory of our colleague and friend, Dr Russell Binions, who passed away unexpectedly during the preparation of this manuscript.

REFERENCES

- Das, S.; Jayaraman, V. SnO_2 : A comprehensive review on structures and gas sensors. *Prog. Mater. Sci.* **2014**, *66*, 112–255.
- Chen, Z.; Pan, D.; Li, Z.; Jiao, Z.; Wu, M.; Shek, C.-H.; Wu, C. M. L.; Lai, J. K. L. Recent Advances in Tin Dioxide Materials: Some Developments in Thin Films, Nanowires, and Nanorods. *Chem. Rev.* **2014**, *114*, 7442–7486.
- Kamat, P. V. Dominance of Metal Oxides in the Era of Nanotechnology. *J. Phys. Chem. Lett.* **2011**, *2*, 839–840.
- Wang, J.; Lian, G.; Si, H.; Wang, Q.; Cui, D.; Wong, C.-P. Pressure-Induced Oriented Attachment Growth of Large-Size Crystals for Constructing 3D Ordered Superstructures. *ACS Nano* **2016**, *10*, 405–412.
- Ma, N.; Suematsu, K.; Yuasa, M.; Kida, T.; Shimano, K. Effect of Water Vapor on Pd-Loaded SnO_2 Nanoparticles Gas Sensor. *ACS Appl. Mater. Interfaces* **2015**, *7*, 5863–5869.
- Bae, J.-Y.; Park, J.; Kim, H. Y.; Kim, H.-S.; Park, J.-S. Facile Route to the Controlled Synthesis of Tetragonal and Orthorhombic SnO_2 Films by Mist Chemical Vapor Deposition. *ACS Appl. Mater. Interfaces* **2015**, *7*, 12074–12079.
- Xu, X.; Zhuang, J.; Wang, X. SnO_2 Quantum Dots and Quantum Wires: Controllable Synthesis, Self-Assembled 2D Architectures, and Gas-Sensing Properties. *J. Am. Chem. Soc.* **2008**, *130*, 12527–12535.
- Zhu, Y.; Guo, H.; Zhai, H.; Cao, C. Microwave-Assisted and Gram-Scale Synthesis of Ultrathin SnO_2 Nanosheets with Enhanced Lithium Storage Properties. *ACS Appl. Mater. Interfaces* **2015**, *7*, 2745–2753.
- Lavanya, N.; Radhakrishnan, S.; Sudhan, N.; Sekar, C.; Leonardi, S. G.; Cannilla, C.; Neri, G. Fabrication of folic acid sensor based on the Cu doped SnO_2 nanoparticles modified glassy carbon electrode. *Nanotechnology* **2014**, *25*, 295501.
- Sarmah, S.; Kumar, A. Optical properties of SnO_2 nanoparticles. *Indian J. Phys.* **2010**, *84*, 1211–1221.
- Chiu, H.-C.; Yeh, C.-S. Hydrothermal Synthesis of SnO_2 Nanoparticles and Their Gas-Sensing of Alcohol. *J. Phys. Chem. C* **2007**, *111*, 7256–7259.
- Wang, X.; Wang, Y.; Tian, F.; Liang, H.; Wang, K.; Zhao, X.; Lu, Z.; Jiang, K.; Yang, L.; Lou, X. From the Surface Reaction Control to Gas-Diffusion Control: The Synthesis of Hierarchical Porous SnO_2

- 732 Microspheres and Their Gas-Sensing Mechanism. *J. Phys. Chem. C*
733 **2015**, *119*, 15963–15976.
- 734 (13) Ding, L.; He, S.; Miao, S.; Jorgensen, M. R.; Leubner, S.; Yan,
735 C.; Hickey, S. G.; Eychmüller, A.; Xu, J.; Schmidt, O. G. Ultrasmall
736 SnO₂ Nanocrystals: Hot-bubbling Synthesis, Encapsulation in Carbon
737 Layers and Applications in High Capacity Li-Ion Storage. *Sci. Rep.*
738 **2014**, *4*, 4647.
- 739 (14) Karmaoui, M.; Ramana, E. V.; Tobaldi, D. M.; Lajaunie, L.;
740 Graça, M. P.; Arenal, R.; Seabra, M. P.; Labrincha, J. A.; Pullar, R. C.
741 High dielectric constant and capacitance in ultrasmall (2.5 nm)
742 SrHfO₃ perovskite nanoparticles produced in a low temperature non-
743 aqueous sol-gel route. *RSC Adv.* **2016**, *6*, 51493–51502.
- 744 (15) Karmaoui, M.; Leonardi, S. G.; Latino, M.; Tobaldi, D. M.;
745 Donato, N.; Pullar, R. C.; Seabra, M. P.; Labrincha, J. A.; Neri, G. Pt-
746 decorated In₂O₃ nanoparticles and their ability as a highly sensitive
747 (<10 ppb) acetone sensor for biomedical applications. *Sens. Actuators*,
748 *B* **2016**, *230*, 697–705.
- 749 (16) Karmaoui, M.; Amaral, J. S.; Lajaunie, L.; Puliyalil, H.; Tobaldi,
750 D. M.; Pullar, R. C.; Labrincha, J. A.; Arenal, R.; Cvelbar, U. Smallest
751 Bimetallic CoPt₃ Superparamagnetic Nanoparticles. *J. Phys. Chem.*
752 *Lett.* **2016**, *7*, 4039–4046.
- 753 (17) Karmaoui, M.; Lajaunie, L.; Tobaldi, D. M.; Leonardi, G.;
754 Benbayer, C.; Arenal, R.; Labrincha, J. A.; Neri, G. Modification of
755 anatase using noble-metals (Au, Pt, Ag): Toward a nanohetero-
756 ojunction exhibiting simultaneously photocatalytic activity and
757 plasmonic gas sensing. *Appl. Catal., B* **2017**, *218*, 370–384.
- 758 (18) Pinna, N.; Neri, G.; Antonietti, M.; Niederberger, M.
759 Nonaqueous Synthesis of Nanocrystalline Semiconducting Metal
760 Oxides for Gas Sensing. *Angew. Chem., Int. Ed.* **2004**, *43*, 4345–4349.
- 761 (19) Sanon, G.; Rup, R.; Mansingh, A. Band-gap narrowing and
762 band structure in degenerate tin oxide (SnO₂) films. *Phys. Rev. B*:
763 *Condens. Matter Mater. Phys.* **1991**, *44*, S672–S680.
- 764 (20) Zhou, W.; Liu, Y.; Yang, Y.; Wu, P. Band Gap Engineering of
765 SnO₂ by Epitaxial Strain: Experimental and Theoretical Investigations.
766 *J. Phys. Chem. C* **2014**, *118*, 6448–6453.
- 767 (21) Chetri, P.; Choudhury, A. Investigation of optical properties of
768 SnO₂ nanoparticles. *Phys. E* **2013**, *47*, 257–263.
- 769 (22) Mendes, P. G.; Moreira, M. L.; Tebcherani, S. M.; Orlandi, M.
770 O.; Andrés, J.; Li, M. S.; Diaz-Mora, N.; Varela, J. A.; Longo, E. SnO₂
771 nanocrystals synthesized by microwave-assisted hydrothermal meth-
772 od: towards a relationship between structural and optical properties. *J.*
773 *Nanopart. Res.* **2012**, *14*, 750.
- 774 (23) Viter, R.; Katoch, A.; Kim, S. S. Grain size dependent bandgap
775 shift of SnO₂ nanofibers. *Met. Mater. Int.* **2014**, *20*, 163–167.
- 776 (24) Sharma, V. An insight into the structural, electrical and optical
777 properties of SnO₂ nanoparticles. *J. Sol-Gel Sci. Technol.* **2017**, *84*,
778 231–238.
- 779 (25) Ahmed, A. S.; Azam, A.; Shafeeq, M. M.; Chaman, M.;
780 Tabassum, S. Temperature dependent structural and optical proper-
781 ties of tin oxide nanoparticles. *J. Phys. Chem. Solids* **2012**, *73*, 943–
782 947.
- 783 (26) Pang, G.; Chen, S.; Koltypin, Y.; Zaban, A.; Feng, S.;
784 Gedanken, A. Controlling the Particle Size of Calcined SnO₂
785 Nanocrystals. *Nano Lett.* **2001**, *1*, 723–726.
- 786 (27) Scardi, P.; Leoni, M. Whole powder pattern modelling. *Acta*
787 *Crystallogr., Sect. A: Found. Crystallogr.* **2002**, *58*, 190–200.
- 788 (28) Leoni, M.; Confente, T.; Scardi, P. PM2K: a flexible program
789 implementing Whole Powder Pattern Modelling. *Z. Kristallogr. Suppl.*
790 **2006**, *2006*, 249–254.
- 791 (29) Scardi, P.; Leoni, M. Whole Powder Pattern Modelling: Theory
792 and Applications. In *Diffraction Analysis of the Microstructure of*
793 *Materials*; Mittemeijer, I. E. J., Scardi, P., Eds.; Springer: Berlin, 2004;
794 pp 51–91.
- 795 (30) Scardi, P.; Leoni, M. Line Profile Analysis: Pattern Modelling
796 versus Profile Fitting. *J. Appl. Crystallogr.* **2006**, *39*, 24–31.
- 797 (31) Scardi, P. Microstructural Properties: Lattice Defects and
798 Domain Size Effects. In *Powder Diffraction: Theory and Practice*;
799 Dinnebier, R. E., Billinge, S. J. L., Eds.; RSC Publishing: Cambridge,
800 2008; pp 376–413.
- (32) Scardi, P.; Leoni, M. Diffraction line profiles from polydisperse
801 crystalline systems. *Acta Crystallogr., Sect. A: Found. Crystallogr.* **2001**,
802 *57*, 604–613.
- (33) Leoni, M.; Martinez-Garcia, J.; Scardi, P. Dislocation effects in
803 powder diffraction. *J. Appl. Crystallogr.* **2007**, *40*, 719–724.
- (34) Leoni, M.; Confente, T.; Scardi, P. PM2K: a flexible program
804 implementing Whole Powder Pattern Modelling. *Z. Kristallogr. Suppl.*
805 **2006**, *2006*, 249–254.
- (35) Scardi, P. Recent advancements in Whole Powder Pattern
806 Modelling. *Z. Kristallogr. Suppl.* **2008**, *2008*, 101–111.
- (36) Doodoo-Arhin, D.; Nuamah, R. A.; Jain, P. K.; Obada, D. O.;
807 Yaya, A. Nanostructured stannic oxide: Synthesis and characterisation
808 for potential energy storage applications. *Results Phys.* **2018**, *9*, 1391–
809 1402.
- (37) Aliev, A. E.; Harris, K. D. M. Probing Hydrogen Bonding in
810 Solids Using Solid State NMR Spectroscopy. In *Supramolecular*
811 *Assembly via Hydrogen Bonds I*; Mingos, D. M. P., Ed.; Springer Berlin
812 Heidelberg: Berlin, Heidelberg, 2004; pp 1–53.
- (38) Wehrli, F. W.; Marchand, A. P.; Wehrli, S. *Interpretation of*
813 *Carbon-13 NMR Spectra*; Wiley: New York, Brisbane, Toronto,
814 Singapore, 1988.
- (39) Breitmaier, E.; Voelter, W. *Carbon-13 NMR Spectroscopy-High*
815 *Resolution Methods and Applications in Organic Chemistry and*
816 *Biochemistry*, 3rd ed.; Wiley-VCH, 1986.
- (40) Aliev, A. E.; Harris, K. D. M. Conformational properties of
817 monosubstituted cyclohexanes in their thiourea inclusion compounds
818 and in solution: variable-temperature one-dimensional and two-
819 dimensional carbon-13 NMR investigations. *J. Am. Chem. Soc.* **1993**,
820 *115*, 6369–6377.
- (41) Tunstall, D. P.; Patou, S.; Liu, R. S.; Kao, Y. H. Size effects in
821 the NMR of SnO₂ powders. *Mater. Res. Bull.* **1999**, *34*, 1513–1520.
- (42) Alla, M.; Lippmaa, E. Resolution limits in magic-angle rotation
822 NMR spectra of polycrystalline solids. *Chem. Phys. Lett.* **1982**, *87*, 30–
823 33.
- (43) Cossement, C.; Darville, J.; Gilles, J.-M.; Nagy, J. B.; Fernandez,
824 C.; Amoureux, J.-P. Chemical shift anisotropy and indirect coupling in
825 SnO₂ and SnO. *Magn. Reson. Chem.* **1992**, *30*, 263–270.
- (44) Clayden, N. J.; Dobson, C. M.; Fern, A. High-resolution solid-
826 state tin-119 nuclear magnetic resonance spectroscopy of ternary tin
827 oxides. *J. Chem. Soc., Dalton Trans.* **1989**, 843–847.
- (45) Ayeshamariam, A.; Ramalingam, S.; Bououdina, M.;
828 Jayachandran, M. Preparation and characterizations of SnO₂ nano-
829 powder and spectroscopic (FT-IR, FT-Raman, UV-Visible and
830 NMR) analysis using HF and DFT calculations. *Spectrochim. Acta*,
831 *Part A* **2014**, *118*, 1135–1143.
- (46) Amalric-Popescu, D.; Bozon-Verduraz, F. Infrared studies on
832 SnO₂ and Pd/SnO₂. *Catal. Today* **2001**, *70*, 139–154.
- (47) Diéguez, A.; Romano-Rodríguez, A.; Vilà, A.; Morante, J. R.
833 The complete Raman spectrum of nanometric SnO₂ particles. *J. Appl.*
834 *Phys.* **2001**, *90*, 1550–1557.
- (48) Sangeetha, P.; Sasirekha, V.; Ramakrishnan, V. Micro-Raman
835 investigation of tin dioxide nanostructured material based on
836 annealing effect. *J. Raman Spectrosc.* **2011**, *42*, 1634–1639.
- (49) Zuo, J.; Xu, C.; Liu, X.; Wang, C.; Wang, C.; Hu, Y.; Qian, Y.
837 Study of the Raman spectrum of nanometer SnO₂. *J. Appl. Phys.* **1994**,
838 *75*, 1835–1836.
- (50) Gupta, S. D.; Gupta, S. K.; Jha, P. K.; Ovsyuk, N. N. A first
839 principles lattice dynamics and Raman spectra of the ferroelastic rutile
840 to CaCl₂ phase transition in SnO₂ at high pressure. *J. Raman Spectrosc.*
841 **2013**, *44*, 926–933.
- (51) Porte, Y.; Maller, R.; Faber, H.; AlShareef, H. N.; Anthopoulos,
842 T. D.; McLachlan, M. A. Exploring and controlling intrinsic defect
843 formation in SnO₂ thin films. *J. Mater. Chem. C* **2016**, *4*, 758–765.
- (52) Ganose, A. M.; Scanlon, D. O. Band gap and work function
844 tailoring of SnO₂ for improved transparent conducting ability in
845 photovoltaics. *J. Mater. Chem. C* **2016**, *4*, 1467–1475.
- (53) Lu, J. G.; Chang, P.; Fan, Z. Quasi-one-dimensional metal oxide
846 materials—Synthesis, properties and applications. *Mater. Sci. Eng., R*
847 **2006**, *52*, 49–91.

- 870 (54) Caglar, Y.; Caglar, M.; Ilican, S.; Yakuphanoglu, F.
871 Determination of the electronic parameters of nanostructure SnO₂/
872 p-Si diode. *Microelectron. Eng.* **2009**, *86*, 2072–2077.
- 873 (55) Abass, A. K.; Al-Liabi, N. A.; Taha, W. A. Optical properties of
874 bromine-doped SnO₂ coatings for solar applications. *Phys. Status*
875 *Solidi A* **1988**, *106*, 613–618.
- 876 (56) Ginley, D. S. *Handbook of Transparent Conductors*; Springer:
877 Boston, MA, 2010.
- 878 (57) Wu, N.-L.; Wang, S.-Y.; Rusakova, I. A. Inhibition of Crystallite
879 Growth in the Sol-Gel Synthesis of Nanocrystalline Metal Oxides.
880 *Science* **1999**, *285*, 1375–1377.
- 881 (58) Tsunekawa, S.; Kang, J.; Asami, K.; Kasuya, A. Blueshifts in the
882 ultraviolet absorption spectra of amphoteric SnO_{2-x} nanocrystalline
883 particles. *J. Appl. Phys.* **2002**, *91*, 10098–10102.
- 884 (59) Zhang, G.; Kim, G.; Choi, W. Visible light driven photocatalysis
885 mediated via ligand-to-metal charge transfer (LMCT): an alternative
886 approach to solar activation of titania. *Energy Environ. Sci.* **2014**, *7*,
887 954–966.
- 888 (60) Wang, X.; Fan, H.; Ren, P.; Li, M. Carbon coated SnO₂:
889 synthesis, characterization, and photocatalytic performance. *RSC Adv.*
890 **2014**, *4*, 10284–10289.
- 891 (61) Klug, H. P.; Alexander, L. E. *X-ray Diffraction Procedures: For*
892 *Polycrystalline and Amorphous Materials*, 2nd ed.; Wiley, 1974; Vol. 1,
893 p 992.
- 894 (62) Williamson, G. K.; Hall, W. H. X-ray line broadening from filed
895 aluminium and wolfram. *Acta Metall.* **1953**, *1*, 22–31.
- 896 (63) Scardi, P.; Leoni, M. Diffraction whole-pattern modelling study
897 of anti-phase domains in Cu₃Au. *Acta Mater.* **2005**, *53*, 5229–5239.
- 898 (64) Caglioti, G.; Paoletti, A.; Ricci, F. P. On resolution and
899 luminosity of a neutron diffraction spectrometer for single crystal
900 analysis. *Nucl. Instrum. Methods* **1960**, *9*, 195–198.
- 901 (65) Koffyberg, F. P. Etch Pits and Dislocations in SnO₂ Crystals. *J.*
902 *Appl. Phys.* **1965**, *36*, 844–849.
- 903 (66) Marfunin, A. S. *Physics of Minerals and Inorganic Materials: An*
904 *Introduction*; Springer, 1979.
- 905 (67) Wooten, F. Plasmons And Characteristic Energy Losses. *Optical*
906 *Properties of Solids*; Academic Press, 1972; Chapter 9, pp 210–224.
- 907 (68) Cory, D. G.; Ritchey, W. M. Suppression of signals from the
908 probe in bloch decay spectra. *J. Magn. Reson.* **1988**, *80*, 128–132.
- 909 (69) Harris, R. K.; Mitchell, T. N.; Nesbitt, G. J. Solid-state tin-119
910 NMR spectroscopy: The first observations of (Tin-119, tin-117)
911 coupling constants. *Magn. Reson. Chem.* **1985**, *23*, 1080–1081.